Target-in-the-loop wavefront sensing and control with a Collett–Wolf beacon: speckle-average phase conjugation

Mikhail A. Vorontsov,[1,2,*] Valeriy V. Kolosov,[2,3] and Ernst Polnau[2]

[1]Intelligent Optics Laboratory, Computational and Information Sciences Directorate, U.S. Army Research Laboratory, Adelphi, Maryland 20783, USA

[2]Intelligent Optics Laboratory, Institute for Systems Research, University of Maryland, College Park, Maryland 20742, USA

[3]Institute of Atmospheric Optics, Russian Academy of Science, Siberian Branch, 1 Akademicheskii av., Tomsk, 634055, Russia

*Corresponding author: mvorontsov@arl.army.mil

Received 9 June 2008; revised 27 August 2008; accepted 11 September 2008; posted 19 September 2008 (Doc. ID 97167); published 27 October 2008

Adaptive optical systems for laser beam projection onto an extended target embedded in an optically inhomogeneous medium are considered. A new adaptive optics wavefront control technique—speckle-average (SA) phase conjugation—is introduced. In this technique mitigation of speckle effects related to laser beam scattering off the rough target surface is achieved by measuring the SA wavefront slopes of the target return wave using a conventional Shack–Hartmann wavefront sensor. For statistically representative speckle averaging we consider the generation of an incoherent light source, referred to here as a Collett–Wolf beacon, directly on the target surface using a rapid steering (scanning) auxiliary laser beam. Our numerical simulations and experiment show that control of the outgoing beam phase using SA phase conjugation can lead to efficient compensation of turbulence effects and results in an increase of the projected laser beam power density on a remote extended target. The impact of both target anisoplanatism and the Collett–Wolf beacon size on adaptive system performance is studied. © 2009 Optical Society of America

OCIS codes: 010.1080, 010.1290, 140.3290, 140.3298, 140.3510.

1. Introduction

It is well known that atmospheric turbulence can severely degrade performance of various optical systems, including the laser beam projection systems for directed energy applications discussed here. These systems are designed to create and maintain a laser spot (target hit spot) of the smallest possible size on a remotely located object (target) in the atmosphere. Compensation (mitigation) of turbulence effects in the laser beam projection systems can be performed by controlling (rapidly shaping) the outgoing laser beam wavefront phase using either adaptive optics (AO) wavefront correctors (deformable and/or segmented mirrors, liquid crystal phase modulators, etc. [1,2]) or nonlinear optics phase-conjugation techniques (four-wave mixing, resonance stimulated Brillouin, or Raman backward scattering [3,4]).

Pursuing the same goals—a decrease of target hit-spot size and its brightness increase—this control of the outgoing beam phase $u(\mathbf{r},t)$ can be achieved using different control algorithms. Here $\mathbf{r}=\{x,y\}$ is the vector in the transversal to the plane of wave propagation direction, and t is time.

The best known is the phase-conjugate (PC) wavefront control algorithm, also referred to here as PC precompensation. The PC precompensation approach is based on the assumption that wavefront phase $\varphi(\mathbf{r},t)$ of the received (target-return) wave at the system's combined receiver and transmitter

0003-6935/09/010A13-17$15.00/0

(transceiver) aperture represents a cumulative sum of the turbulence-induced phase disturbances accumulated along the propagation path (along optical axis z) from the target ($z = L$) to the transceiver ($z = 0$) planes and hence can be compensated (precompensated) using conjugation of the return-wave phase $\varphi(\mathbf{r}, t)$ that is measured inside the system transceiver aperture [1,5]. The ideal (infinite spatial resolution) PC precompensation control can be then represented in the following simple form $u(\mathbf{r}, t) = -\varphi(\mathbf{r}, t)$.

The outgoing beam precompensation can also be achieved using conjugation of the return-wave complex amplitude $\psi_0(\mathbf{r}, t)$. In this approach, the complex amplitude of the outgoing wave $A_0(\mathbf{r}, t)$ obeys the field-conjugation (FC) condition $A_0(\mathbf{r}, t) = \gamma\psi^*{}_0(\mathbf{r}, t)$, where γ is the coefficient proportional to the outgoing beam power [6–9].

In the phase aberration precompensation technique known as model-free metric optimization AO, the outgoing beam phase control is based on optimization of specially selected return-wave characteristics (metrics), such as return-wave power inside the receiver aperture (power-in-the-bucket metric J_{PIB}) [10], and sharpness of the hit-spot image as described by different sharpness functions (metrics J_{SF}) [11–13]. It is assumed that these metrics are monotonically dependent on the characteristics of the target hit-spot brightness, and hence their optimization results in the desired hit-spot brightness increase [14,15].

It is important to note that both wavefront control techniques (PC/FC) and optimization of metrics J_{PIB} and J_{SF}) are based on the assumption of a small (unresolved or point-source) target or beacon (glint) on an extended target surface. The target (glint) can be considered as unresolved if its characteristic size b_T is smaller than the diffraction-limited hit-spot radius b^{dif}.

In this paper we consider the more general and, for many practical applications, more interesting case of an extended (resolved) target assuming that $b_T \gg b^{\mathrm{dif}}$. For resolved targets, the return-wave complex amplitude $\psi_0(\mathbf{r}, t)$ is dependent not only on the propagation medium inhomogeneities but also on the target shape and surface roughness.

The outgoing beam scattering off an extended target with a randomly rough surface results in strong speckle-modulation of the return wave [16–18]. This speckle modulation is the major problem for both the PC/FC and metric optimization wavefront control techniques [6,19,20].

In the presence of speckle modulation, the return-wave phase $\varphi(\mathbf{r}, t) = \varphi_{\mathrm{at}}(\mathbf{r}, t) + \varphi_s(\mathbf{r}, t)$ is composed of two terms (components): the turbulence-induced phase $\varphi_{\mathrm{at}}(\mathbf{r}, t)$ and the phase noise term $\varphi_s(\mathbf{r}, t)$ that results from the outgoing beam scattering off the target surface. For mitigation of the turbulence-induced phase component $\varphi_{\mathrm{at}}(\mathbf{r}, t)$, the phase noise $\varphi_s(\mathbf{r}, t)$ should be somehow removed from the return-wave phase measurements.

Consider briefly several techniques that can be applied for either removing or at least reducing speckle effects. In the case of a rapidly spinning extended target, the negative impact of speckles can be potentially mitigated using optimization of either metrics obtained by time averaging of speckle modulation (speckle-averaged sharpness functions [13,21]) or metrics whose values are dependent on statistical characteristics of the speckle field, which are sensitive to the target hit-spot size (speckle metrics [17,18,20]). Nevertheless, practical implementation of wavefront control using optimization of these metrics is quite limited. Because of the relatively slow convergence of the metric optimization process, speckle-modulation averaging and speckle-metric measurements should be performed during a relatively short time (typically a few microseconds), and hence this technique can only be applied for laser beam projection on rapidly spinning targets (see [20]).

In the well-known laser guide-star technique, the speckle-modulation problem does not exist since the phase measurements are performed using an auxiliary incoherent light source (guide-star) generated with an additional laser [22–24]. Under ideal conditions for guide-star operation, this additional laser beam can be focused in close vicinity to the target, thus creating an intense light backscattering. The backscattering occurs inside a volume of air (guide-star volume), which is bounded by the focused laser beam waist. This volume forms a light source used for wavefront measurements and PC-based precompensation of the outgoing beam.

It is commonly assumed that the guide-star volume is small enough to be considered as an unresolved (point-source) beacon whose size is smaller than the diffraction-limited beam size. The optical wave that originates from the guide-star beacon propagates to the transceiver aperture. Wavefront phase $\varphi_{\mathrm{gs}}(\mathbf{r}, t)$ of this wave is measured by a wavefront sensor. In the guide-star AO technique, phase $\varphi_{\mathrm{gs}}(\mathbf{r}, t)$ is used for the outgoing beam PC precompensation in the form $u(\mathbf{r}, t) = -\varphi_{\mathrm{gs}}(\mathbf{r}, t)$.

Note that the coherence time τ_c of the guide-star light source is negligibly smaller than the following three major characteristic times on which the AO system operation depends: τ_{ph}, τ_{AO}, and τ_{at}. Here, τ_{ph} is the integration time of a photosensor used for return field sensing, τ_{AO} is the response time of the AO control system, and τ_{at} is atmospheric turbulence characteristic time. For an adaptive beam projection system based on the guide-star technique, the following inequalities are fulfilled:

$$\tau_c \ll \tau_{\mathrm{ph}} < \tau_{\mathrm{AO}} < \tau_{\mathrm{at}}. \tag{1}$$

This condition plays an important role in the following analysis.

The laser guide star approach has several well-known shortcomings related to the presence of uncensored wavefront aberration $\varphi_{\mathrm{un}}(\mathbf{r}, t)$ that results from a mismatch in the guide-star and target positions—effects often referred to as angular and focus (conical) anisoplanatisms [24]. In addition, the turbulence-induced widening of the propagated laser beam can lead to the significant increase of the guide-star volume. As a result, the formed light source cannot be considered as an unresolved beacon, and hence conjugation of the measured phase $\varphi_{gs}(\mathbf{r}, t)$ can give only a partial precompensation of the turbulence effects.

In principle, the speckle-free incoherent (partially coherent) reference light source for wavefront measurements can be created directly on the target surface (target-surface guide star) using an auxiliary laser illuminator system based on an array of incoherently combined lasers. Still, due to the turbulence-induced laser beam(s) widening, beam jitter, and beam-combining misalignments, the obtained beacon commonly represents an extended light source. As a result the measured phase $\varphi_{gs}(\mathbf{r}, t)$ can be "corrupted" by the presence of the phase component associated with the incoherently illuminated area at the target surface.

In this paper we consider a different approach for the mitigation of speckle effects in adaptive laser beam projection systems. The target-surface incoherent beacon is created using either the projected laser beam itself or a single auxiliary laser illuminator beam. In the last case the laser illuminator is used for wavefront sensing and adaptive precompensation of the projected beam. In general terms this approach uses a difference in the characteristic time scales (either existing or artificially created) of the return-wave modulation caused by either the outgoing beam scattering off the target rough surface (time scale τ_s) or by the atmospheric turbulence and/or AO system operation (time scales τ_{AO} and τ_{at}).

We assume here that the characteristic time τ_s is (or can be made) sufficiently shorter than the corresponding characteristic times τ_{AO} and τ_{at}, so that the following inequalities, referred to here as the speckle-averaging condition, are fulfilled:

$$\tau_s \ll \tau_{ph} < \tau_{AO} < \tau_{at}. \quad (2)$$

The inequality $\tau_s \ll \tau_{ph}$ indicates that during the integration time τ_{ph} of the AO system sensor, a large number of speckle-field realizations pass through the receiver aperture, and hence the obtained return-wave measurements correspond to the speckle field time-averaged characteristics. These measurements are referred to here as the *speckle-average (SA) measurements* [21].

From condition (2) it follows that the photodetector integration time τ_{ph} is significantly shorter than the characteristic times τ_{AO} and τ_{at}. This is the case when both turbulence- and AO-induced phase variations can be considered as stationary ("frozen") during SA measurements.

The inequalities (2) are automatically fulfilled for laser beam projection onto a fast-spinning extended target with a randomly rough surface. The return-wave speckle-pattern update time $\tau_s \sim b_s/v_T$ is then associated with the target-surface roughness realizations update inside the target hit-spot illuminated area, where b_s is a characteristic beam (hit-spot) size at the target surface, and v_T is the target surface velocity [21].

For a stationary (or slow-moving/spinning) target, the speckle-averaging condition (2) can be artificially imposed by introducing small amplitude, rapid steering (scanning) of the outgoing laser beam, resulting in the target hit-spot displacements inside a bounded region of the target. These fast hit-spot displacements lead to the roughness realizations update inside the illuminated area of the target surface and hence cause a rapid update of the speckle-field pattern realization inside the receiver aperture of the wavefront sensor.

To obtain a statistically representative ensemble of speckle-field realizations at the receiver plane, the amplitude of the hit-spot displacement b_{scan} should be larger than the target hit spot b_s. At the same time, the distance b_{scan} should be smaller than the isoplanatic patch b_{isp} to prevent unwanted averaging of the atmospheric turbulence-induced phase distortions within the propagation medium volume of the steered laser beam.

At the time scale of the sensor integration time $\tau_{ph} \gg \tau_s$, referred to here as slow time, the quasi-monochromatic optical field scattered off an extended target with a rapidly moving diffusely reflective surface can be associated with an optical wave originating from an extended incoherent (partially coherent) light source known as the Collett–Wolf light source [25–27]. In this paper we use the term the *Collett–Wolf beacon* since this light source represents a beacon used for the outgoing beam phase precompensation.

For rapidly spinning cylindrical-shape targets with radius $r_T \gg b_s$, the Collett–Wolf beacon characteristics (size and brightness) are determined by the instantaneous target-plane intensity distribution $I_T(\mathbf{r}, t)$. For the case of outgoing beam scanning, the corresponding Collett–Wolf beacon depends on the scanning beam trajectory.

The first question to ask is how we can define the phase of an optical wave that originates from the Collett–Wolf beacon? In Section 2, this phase (*SA phase*) defined through the return-wave SA measurements performed with an ideal (infinite-resolution) Shack–Hartmann (SH) wavefront sensor. It can be shown (see [21]) that if the speckle-averaging conditions (2) are satisfied, then the function $\Phi(\mathbf{r}, t)$ that is reconstructed from SA measurements describes a surface that is orthogonal to the return-wave energy-flux vector at each point $\mathbf{r}$ of the receiver aperture. In the speckle-average phase-conjugation (SA PC) technique described, the control of the outgoing beam phase $u(\mathbf{r}, t)$ is based on conjugation of the SA phase $\Phi(\mathbf{r}, t)$; that is, $u(\mathbf{r}, t) = -\Phi(\mathbf{r}, t)$.

Note the similarity of the inequalities (1) and (2) that are required for adaptive wavefront phase precompensation using either an auxiliary spatially incoherent beacon (guide star or surface guide star), or the Collett–Wolf beacon. This similarity implies that the approach presented here can also be applied to analysis of AO techniques based on the use of an extended laser guide-star volume or a target-surface guide star. Nevertheless, for definitiveness we further consider only the Collett–Wolf beacon associated with the outgoing beam scattering off the Lambertian target surface.

The mathematical and numerical models of an adaptive laser beam projection system based on the Collett–Wolf beacon are presented in Section 3 for targets with the Lambertian surface roughness. The numerical analysis of the system performance is performed using both the MC and BF methods.

In Section 4 the efficiency of the SA PC precompensation is analyzed using numerical simulations. It is shown that for a resolved and moving (spinning) target the SA PC precompensation leads to the efficient compensation of atmospheric turbulence-induced phase aberrations and the corresponding increase of target hit-spot brightness.

Results of the bench-top experiments with the adaptive beam projection system based on the SA PC wavefront control technique are presented in Section 5.

2. Speckle-Average Wavefront Phase

A. Instantaneous Wavefront Slopes

Consider an outgoing laser beam projection onto an extended target with the Lambertian surface using an AO system. Represent the complex amplitude $\psi(\mathbf{r},z,t)$ of the return field at the receiver aperture plane in the form

$$\psi(r,z=0,t) \equiv \psi_0(\mathbf{r},t) = I_0{}^{1/2}(\mathbf{r},t)\exp[i\varphi(\mathbf{r},t)], \quad (3)$$

where $\varphi(\mathbf{r},t)$ and $I_0(\mathbf{r},t)$ are the return-wave instantaneous phase and intensity. We assume that the adaptive system is equipped with a SH wavefront sensor located in the image plane of the beam projection telescope pupil and that the complex amplitude of the wave entering this sensor coincides with $\psi_0(\mathbf{r},t)$.

The SH sensor is composed of an array of N densely packed small lenses (lenslet array) with identical focal length F and a photoarray in the lenslet array focal plane [28]. The sensor measures the return-wave centroid vectors $\{\mathbf{r}_j^c\}$ corresponding to the first moment of the intensity distributions in the focal plane of the jth lenslet, where $j=1,\ldots,N$. The centroid vectors $\{\mathbf{r}_j^c\}$ are used for calculations of the phase gradient vectors $\{\nabla_{\varphi_j}(t)\}$ or the corresponding slope vectors $\{\alpha_j(t)\}$:

$$\{\alpha_j(t)\} \equiv \{k^{-1}\nabla_{\varphi_j}(t)\} = \{r_j^c(t)\}/F, (j=1.,\ldots,N), \quad (4)$$

where $k=2\pi/\lambda$ is wavenumber [1,28].

In the limiting case of $N\to\infty$ corresponding to high-resolution wavefront sensing considered here, the slope vectors in Eq. (4) can be replaced by the vector function

$$\boldsymbol{\alpha}(\mathbf{r},t) = \frac{1}{k}\nabla\varphi(\mathbf{r},t). \quad (5)$$

The speckle-field phase $\varphi(\mathbf{r},t)$ can then be reconstructed by integrating the measured slopes $\boldsymbol{\alpha}(\mathbf{r},t)$ [30]. It can be shown (see [21]) that vector function $\boldsymbol{\alpha}(\mathbf{r},t)$ can be represented in the following form:

$$\boldsymbol{\alpha}(\mathbf{r},t) = \mathbf{S}_\perp(\mathbf{r},t)/I_0(\mathbf{r},t), \quad (6)$$

where vector

$$\mathbf{S}_\perp(\mathbf{r},t) = \frac{1}{2ik}\left[\psi_0^*(\mathbf{r},t)\nabla\psi_0(\mathbf{r},t) - \psi_0(\mathbf{r},t)\nabla\psi_0^*(\mathbf{r},t)\right] \quad (7)$$

coincides with the transverse component of the energy-flux vector (Poynting vector) [30].

B. Speckle-Average Slopes

Assume now that the outgoing laser beam is projected onto an extended planar target with a rapidly moving randomly rough surface, so that the speckle-averaging condition (2) is satisfied. The speckle-averaging measurements performed using the high-resolution SH wavefront sensor result in the time-averaged slope vector function $\langle\boldsymbol{\alpha}(\mathbf{r},t)\rangle$. By substituting the time averaging in the expressions (4) and (5) by statistical averaging over an ensemble of the return-wave realizations (denoted here as $\langle\rangle_s$, we obtain [21]

$$\langle\boldsymbol{\alpha}(\mathbf{r},t)\rangle_s = \frac{\langle\mathbf{S}_\perp(\mathbf{r},t)\rangle_s}{\langle I_0(\mathbf{r},t)\rangle_s} = \frac{\langle\psi_0^*(\mathbf{r},t)\nabla\psi_0(\mathbf{r},t)\rangle_s - \langle\psi_0(\mathbf{r},t)\nabla\psi_0^*(\mathbf{r},t)\rangle_s}{2ik\langle\psi_0(\mathbf{r},t)\psi_0^*(\mathbf{r},t)\rangle_s}. \quad (8)$$

Here we assumed that the intensity $I_0(\mathbf{r},t)$ and phase gradient $\nabla\varphi(\mathbf{r},t)$ are statistically independent functions.

This expression can be further transformed using the mutual correlation function (MCF) of the return random field defined as

$$\Gamma_0(\mathbf{r}_1,\mathbf{r}_2,t) \equiv \langle\psi_0(\mathbf{r}_1,t)\psi_0^*(\mathbf{r}_2,t)\rangle_s, \quad (9)$$

where $\mathbf{r}_1$ and $\mathbf{r}_2$ are vectors at the receiver plane [21,26]. In the sum and difference coordinates $\mathbf{R}=(\mathbf{r}_1+\mathbf{r}_2)/2$ and $\boldsymbol{\rho}=(\mathbf{r}_1-\mathbf{r}_2)$ from Eq. (9) we obtain

$$\Gamma_0(\rho,\mathbf{R},t) \equiv \langle\psi_0(\mathbf{R}+\rho/2,t)\psi_0^*(\mathbf{R}-\rho/2,t)\rangle_s. \quad (10)$$

Note, that the MCF in Eqs. (9) and (10) depends on the "slow" time t that characterizes temporal processes occurring on the time scale of adaptive system operation and atmospheric effects.

Using Eq. (10) the SA slopes $\langle \boldsymbol{\alpha}(\mathbf{r},t)\rangle_s$ in Eq. (8) can be represented in the following equivalent form [21]:

$$\langle \boldsymbol{\alpha}(\mathbf{R},t)\rangle_s \equiv \langle \mathbf{S}_\perp(\mathbf{R},t)\rangle_s / \langle I_0(\mathbf{R},t)\rangle_s = (ik)^{-1} \times \nabla_\rho \ln \Gamma_0(\boldsymbol{\rho}\to 0,\mathbf{R}), \quad (11)$$

where the notation $\boldsymbol{\rho}\to 0$ indicates that the gradient over the difference vector $\boldsymbol{\rho}$ is computed at the point $\boldsymbol{\rho}=0$. This expression can be further simplified using the known relationship between the mutual correlation function $\Gamma_0(\boldsymbol{\rho},\mathbf{R},t)$ and the BF $B_0(\theta,\mathbf{R},t)$ [21,26]. The latest is defined by the Fourier transform of the MCF (10) over the difference coordinate $\boldsymbol{\rho}$:

$$B_0(\boldsymbol{\theta},\mathbf{R},t) = \frac{1}{(2\pi)^2}\int \Gamma_0(\boldsymbol{\rho},\mathbf{R},t)\exp(-ik\boldsymbol{\theta}\rho)\mathrm{d}^2\rho, \quad (12)$$

where $\boldsymbol{\theta}$ is the Fourier transform angular coordinate vector. Using this expression from Eq. (11) we finally obtain [21]

$$\langle \boldsymbol{\alpha}(\mathbf{r},t)\rangle_s = \frac{\int \boldsymbol{\theta} B_0(\boldsymbol{\theta},r,t)\mathrm{d}^2\boldsymbol{\theta}}{\int B_0(\boldsymbol{\theta},r,t)\mathrm{d}^2\boldsymbol{\theta}}. \quad (13)$$

The right-hand side of this expression describes the BF angular momentum. The representation of the SA slope vector function $\langle \boldsymbol{\alpha}(\mathbf{r},t)\rangle_s$ in Eq. (13) is used as the BF angular momentum in the numerical analysis of the adaptive beam projection systems in Section 3.

C. Speckle-Average Phase

Assume that the SA slope function $\langle \boldsymbol{\alpha}(\mathbf{r},t)\rangle_s$ is a path-independent vector field. In this case the SA slope function $\langle \boldsymbol{\alpha}(\mathbf{r},t)\rangle_s$ can be represented as a gradient of an auxiliary potential function $\Phi(\mathbf{r},t)$ [30]: $\langle \boldsymbol{\alpha}(\mathbf{r},t)\rangle_s = \nabla\Phi(\mathbf{r},t)/k$.The function $\Phi(\mathbf{r},t)$ can be reconstructed from the SA slopes $\langle \boldsymbol{\alpha}(\mathbf{r},t)\rangle_s$, similar to how the instantaneous phase $\varphi(\mathbf{r},t)$ is reconstructed from the instantaneous wavefront slopes $\boldsymbol{\alpha}(\mathbf{r},t)$. For this reason, $\varphi(\mathbf{r},t)$ can be formally referred to as the *speckle-average phase* associated with an optical wave originating from an extended Collett–Wolf beacon.

To illustrate the physical meaning of the SA phase, compare Eqs. (8) and (14) for $\langle \boldsymbol{\alpha}(\mathbf{r},t)\rangle_s$. As a result, we obtain

$$\frac{\langle \mathbf{S}_\perp(\mathbf{r},t)\rangle_s}{\langle I_0(\mathbf{r},t)\rangle_s} = \frac{1}{k}\nabla\Phi(\mathbf{r},t). \quad (15)$$

This equality shows that gradient $\nabla\Phi(\mathbf{r},t)$ is collinear to the direction of the averaged energy-flux vector $\langle \mathbf{S}_\perp(\mathbf{r},t)\rangle_s$. Correspondingly at each point $\mathbf{r}$ of the transceiver aperture, the plane tangent to the surface defined by the function $\Phi(\mathbf{r},t)$, is orthogonal to the averaged energy-flux vector $\langle \mathbf{S}_\perp(\mathbf{r},t)\rangle_s$.

As pointed out in [21], the SA phase $\Phi(\mathbf{r},t))$ may not coincide with the phase $\langle\varphi(\mathbf{r},t)\rangle_s$ corresponding to speckle averaging of the instantaneous phases $\{\varphi(\mathbf{r},t)\}$ obtained for different realizations of target-surface roughness.

D. Speckle-Average Phase Conjugation

Consider an application of the SA phase $\Phi(\mathbf{r},t)$ for control of the outgoing beam phase. Similar to the conventional phase-conjugate precompensation algorithm, we assume the following wavefront control rule:

$$u(\mathbf{r},t) = -\Phi(\mathbf{r},t), \quad (16)$$

referred to here as the SA PC. Note that for a point-source target, functions $\Phi(\mathbf{r},t)$ and $\varphi(\mathbf{r},t)$ are identical, and correspondingly the precompensation rule (16) coincides with conventional phase conjugation.

The key question is if the replacement of the instantaneous phase function $\varphi(\mathbf{r},t)$ in the PC control algorithm by the SA phase $\Phi(\mathbf{r},t)$ results in improvement of the laser beam projection performance?

Consider first a special case that can be analyzed analytically—the adaptive laser beam projection onto an extended target with a rapidly moving extended Lambertian surface in the presence of a single thin phase-distorting layer located at the pupil plane (pupil-plane phase screen)[21]. This phase screen introduces phase aberration $\varphi_{\mathrm{at}}(\mathbf{r},t)$ into both the outgoing and received waves. The incoherent extended beacon (Collett–Wolf beacon) is then defined by the target-plane intensity distribution for the outgoing beam $I_T(\mathbf{r},t) = |A(\mathbf{r},z=L,t)|^2$.

As shown in [21] the SA phase $\Phi(\mathbf{r},t)$ can then be derived analytically:

$$\Phi(\mathbf{r},t) = \varphi_{\mathrm{at}}(\mathbf{r},t) + \varphi_q(\mathbf{r}) + \varphi_{\mathrm{tilt}}(\mathbf{r},t). \quad (17)$$

Here $\varphi_q(\mathbf{r}) = -k\mathbf{r}^2/(2L)$ is the quadratic phase component corresponding to the divergent spherical (parabolic) wavefront with the curvature radius, and $\varphi_{\mathrm{tilt}}(\mathbf{r},t) = (k/L)\mathbf{r}_c(t)\mathbf{r}$ is the wavefront tilt component. Function $\varphi_{\mathrm{tilt}}(\mathbf{r},t)$ depends on the beam centroid vector

$$\mathbf{r}_c(t) = \frac{\int \mathbf{r} I_T(\mathbf{r},t)\mathrm{d}^2\mathbf{r}}{\int I_T(\mathbf{r},t)\mathrm{d}^2\mathbf{r}}. \quad (18)$$

The SA PC precompensation can then be represented in the form

$$u(\mathbf{r},t) = -\Phi(\mathbf{r},t) = u^{\mathrm{opt}}(\mathbf{r},t) - \varphi_{\mathrm{tilt}}(\mathbf{r},t), \quad (19)$$

where $u^{\mathrm{opt}}(\mathbf{r},t) = -\varphi_{\mathrm{at}}(\mathbf{r},t) - \varphi_q(\mathbf{r})$ is the phase corresponding to the ideal (optimal) compensation of the pupil-plane phase aberration $\varphi_{\mathrm{at}}(\mathbf{r},t)$. Thus SA PC precompensation results in the formation of the diffraction-limited spot on the extended target surface. The target hit-spot centroid coincides with the centroid for the target hit-spot intensity prior to phase precompensation [21].

In Sections 3 and 4, using numerical simulations, we consider a more general case of SA PC precompensation assuming that the laser beam propagation occurs in an extended phase distorting medium corresponding to the Kolmogorov turbulence model (propagation through deep turbulence).

The following three beam-projection scenarios are analyzed. First (Section 3.C), we consider beam projection onto a planar extended target with a rapidly moving Lambertian surface. At each fixed time $t = t_0$ (slow time), the Collett–Wolf beacon is then defined by the target-plane intensity distribution $I_T(\mathbf{r}, t_0)$. This beacon is used for the SA PC wavefront control of the outgoing beam.

Second (Section 3.D), to investigate effects related solely to the beacon size, we assumed a single-pass atmospheric propagation of an optical wave that originates from a stationary incoherent extended light source in the form of a cigar or square (stationary beacons) placed at the target plane. The corresponding Collett–Wolf stationary beacons of various sizes are used for SA PC precompensation.

Third (Section 4.B), we analyze an outgoing beam scattering off a stationary extended target with a Lambertian surface. The Collett–Wolf beacon is then created by using a small-amplitude periodic rapid angular steering of an auxiliary laser beam.

3. Speckle-Average Phase Computation

A. Mathematical Model

Propagation of the outgoing and return waves in an optically inhomogeneous medium can be described by a system of parabolic wave equations for the complex amplitudes $A(\mathbf{r}, z, t)$ and $\psi(\mathbf{r}, z, t)$ [30,21]:

$$2ik \frac{\partial A(\mathbf{r}, z, t)}{\partial z} = \nabla_\perp^2 A(\mathbf{r}, z, t) + 2k^2 n_1(\mathbf{r}, z, t) A(\mathbf{r}, z, t), \tag{20}$$

$$-2ik \frac{\partial \psi(\mathbf{r}, z, t)}{\partial z} = \nabla_\perp^2 \psi(\mathbf{r}, z, t) + 2k^2 n_1(\mathbf{r}, z, t) \psi(\mathbf{r}, z, t), \tag{21}$$

where $0 \le z \le L$, $\nabla_\perp^2 = \partial^2/\partial^2 x + \partial^2/\partial^2 y$ is the Laplacian operator over the transversal coordinates and $n_1(\mathbf{r}, z, t)$ is a function describing spatiotemporal dynamics of refractive index fluctuations.

Represent the outgoing beam complex amplitude at the transceiver plane in the form

$$A(\mathbf{r}, z = 0, t) = A_0(\mathbf{r}) \exp[iu(\mathbf{r}, t)], \tag{22}$$

where $A_0(\mathbf{r})$ and $u(\mathbf{r})$ are the amplitude and the controlling wavefront phase, respectively.

The scattering of the outgoing beam off the target with a randomly uniform and planar surface is described by the following simplified model [21,31]:

$$\psi(\mathbf{r}, z = L, t) = T(\mathbf{r}, t) A(\mathbf{r}, z = L, t), \tag{23}$$

where $T(\mathbf{r}, t) = V_0 \exp[i\xi(\mathbf{r}, t)]$ is the extended-target complex scattering coefficient, and $V_0 = \text{constant}$. The stationary, isotropic random function $\xi(\mathbf{r}, t)$ describes the phase modulation that results from the outgoing wave scattering off the target rough surface. For the Lambertian surface considered, $\xi(\mathbf{r}, t)$ is the delta-correlated function.

B. Monte Carlo and Brightness Function Techniques

Numerical modeling of the laser beam projection system was performed using both the MC and the recently developed BF techniques [18,21]. The MC approach is based on direct numerical integration of wave-optics equations (20) and (21) with the boundary conditions (22) and (23) at the transceiver and target planes.

For computation of the SA phase $\Phi(\mathbf{r}, t)$ at fixed time $t = t_0$ using the MC approach, the propagation equations (20) and (21) were integrated with the unchanged "frozen" optical inhomogeneities [function $n_1(\mathbf{r}, z, t_0)$ in Eqs. (20) and (21)] but with a large number N_s of random realizations of the target random surface roughness [function $\xi(\mathbf{r}, t_0)$ in Eq. (23)]. The obtained speckle-field realizations $\{\psi_0(\mathbf{r}, t_0)\}$ were used for numerical estimation of the SA slopes $\langle \boldsymbol{\alpha}(\mathbf{r}, t_0) \rangle_s$ using Eq. (8). The number of random realizations of the target random surface roughness N_s was chosen to be sufficiently large (50–100) to achieve an accurate approximation (with less than 10% error) of the slope function $\langle \boldsymbol{\alpha}(\mathbf{r}, t_0) \rangle_s$. The SA phase $\Phi(\mathbf{r}, t_0)$ was calculated from the SA slopes using numerical integration of Eq. (14).

Since the MC technique is extremely computationally expensive, in the numerical simulations described in Sections 3 and 4, this approach was primarily used only for independent evaluation of the results obtained with the BF method. In the BF method, the parabolic equation (20) and the boundary condition (22) were used for calculation of the intensity distribution on the target surface $I_T(\mathbf{r}, t_0) = |A(\mathbf{r}, L, t_0)|^2$ corresponding to "frozen" optical inhomogeneities. This step is identical in both the MC and BF methods. The principal difference between these two methods is in computation of the slope function $\langle \boldsymbol{\alpha}(\mathbf{r}, t_0) \rangle_s$.

To illustrate the BF method, consider first beam projection onto an extended target with rapidly moving Lambertian surface roughness (e.g., a spinning cylindrical target) and assume that the speckle-averaging conditions (2) are fulfilled. The slope function $\langle \boldsymbol{\alpha}(\mathbf{r}, t_0) \rangle_s$ in the BF method is calculated using Eq. (13) for the BF of the return field $B_0(\boldsymbol{\theta}, \mathbf{R}, t_0)$ at the transceiver plane $z = 0$. Similar to the MC method, the SA phase $\Phi(\mathbf{r},t)$ is further calculated by integration of the slope function $\langle\boldsymbol{\alpha}(\mathbf{r},t_0)\rangle_s$ [Eq. (8)].

As shown in [21], the BF at the receiver plane $B_0(\boldsymbol{\theta},\mathbf{R},t_0)$ can be obtained by integration of the following equations for the BF trajectories (rays) $\{\mathbf{R}(z,t),\boldsymbol{\theta}(z,t)\}$:

$$\frac{\mathrm{d}\mathbf{R}(z,t)}{\mathrm{d}z}=\boldsymbol{\theta}(z,t),\qquad \frac{\mathrm{d}\boldsymbol{\theta}(z,t)}{\mathrm{d}z}=-\nabla_{\mathbf{R}}n_1(\mathbf{R},z,t). \quad (24)$$

The first equation defines $\boldsymbol{\theta}$ as a vector tangent to the trajectory along which the BF is a constant, while the second equation describes evolution of the tangent vector along the optical axis caused by optical inhomogeneities. Equations (24) link the BF at the receiver plane $B_0(\boldsymbol{\theta},\mathbf{R},t_0)$ with the corresponding values of the BF $B_L(\boldsymbol{\theta},\mathbf{R},t_0)$ at the target so that at each point of the BF trajectory we have $B_0(\boldsymbol{\theta},\mathbf{R},t_0)=B_L(\boldsymbol{\theta},\mathbf{R},t_0)$.

Assuming that the BF $B_L(\boldsymbol{\theta},\mathbf{R},t_0)$ at the target plane and optical inhomogeneities [function $n_1(\mathbf{r},z,t_0)$] are known, numerical integration of the ray equations (24) results in the desired BF values $B_0(\boldsymbol{\theta},\mathbf{R},t_0)$ at the receiver plane.

The function $B_L(\boldsymbol{\theta},\mathbf{R},t_0)$ defines the boundary condition for the BF trajectories at the target plane. This function can be obtained from the beam scattering condition (23). It can be shown (see [21]) that for a target with a planar Lambertian surface, function $B_L(\boldsymbol{\theta},\mathbf{R},t_0)$ depends on the outgoing beam target-plane intensity distribution

$$B_L(\boldsymbol{\theta},\mathbf{R},t_0)=cI_T(\mathbf{R},t_0), \quad (25)$$

where $c>0$ is a constant insignificant for this analysis. The boundary condition (25) coincides with the corresponding boundary condition for a spatially incoherent light source whose brightness is described by function $I_T(\mathbf{R},t_0)$. This incoherent light source defines the corresponding Collett–Wolf beacon. Note that the actual optical waves originating from either the incoherent light source or the outgoing beam scattering off the target surface are quite different. Nevertheless, under the same propagation conditions, phase function $\psi_{\mathrm{CW}}(\mathbf{r},t)$ corresponding to the incoherent light source with brightness $I_T(\mathbf{r},t_0)$ (Collett–Wolf beacon) and function $\Phi(\mathbf{r},t)$ reconstructed from the time-averaged slopes $\langle\boldsymbol{\alpha}(\mathbf{r},t_0)\rangle$ of the return wave coincide.

From the computational viewpoint, the brightness method is significantly more efficient compared with the MC technique mostly because the BF technique does not require multiple integrations of the return-wave propagation equation (21) to obtain a statistically representative ensemble of the random complex amplitudes $\{\psi_0(\mathbf{r},t_0)\}$ required for calculation of SA slopes $\langle\boldsymbol{\alpha}(\mathbf{r},t_0)\rangle_s$. Comparison of both MC and BF methods is presented in Ref. [18].

In the numerical simulations we used the outgoing beam with the amplitude described by the normalized super-Gaussian function $A_0(\mathbf{r})=\exp[-(r^2/a_0^2)^{16}]$ of radius a_0 (flat-top beam).

The parabolic phase $u(\mathbf{r},t=0)=u_0(\mathbf{r})=kr^2/(2L)$ was used as the outgoing beam phase prior to SA phase conjugation.

Propagation of the flat-top beam with phase $u_0(\mathbf{r})$ in vacuum results in the diffraction-limited intensity distribution at the target plane described by the Airy function [32]:

$$I_T^{\mathrm{Airy}}(\mathbf{r})=I_T^0\left[\frac{2J_1(\mathrm{kra}_0/L)}{\mathrm{kra}_0/L}\right]^2, \quad (26)$$

where I_T^0 is a normalization factor. The diffraction-limited hit-spot radius $b^{\mathrm{dif}}=3.83L/(ka_0)$ is defined by the first zero of the Airy function (26). The intensity distribution (26) is shown in Fig. 1 (the picture in the top left corner) for the propagation distance $L=0.05\,\mathrm{Ka}_0^2$. Note that the distance L used in computations was fixed.

The computations were performed using a numerical grid with $N\times N=512\times 512$ pixels. The transceiver aperture of diameter $D=2\,a_0$ was located in the grid central area of diameter $N/4$ pixels.

The atmospheric turbulence was modeled by a set of $N_{\mathrm{ph}}=20$ equally distanced along the propagation path, random phase screens with statistical characteristics corresponding to the Kolmogorov power spectra [33]. This number of phase screens was selected to ensure less than 5% variation in the averaged target-plane intensity distribution with an additional increase of the number of phase screens used. The turbulence strength was characterized by the ratio D/r_0 of the transceiver aperture diameter D to the Fried parameter r_0 for the plane wave [34].

Equations (24) for the BF trajectories were integrated for each grid point inside the transceiver aperture using a bundle of 150×150 rays with initial angular vectors $\boldsymbol{\theta}=\{\theta_x,\theta_y\}$ belonging to a square angular region of size $-\theta_0<\theta_{xy}<\theta_0$, where $\theta_0=1.5(b_s^{C-W}/L)$ and b_s^{C-W} is the characteristic size of the Collett–Wolf beacon at the target surface.

C. Collett–Wolf Beacon for a Rapidly Scanning Laser Beam

Assume now that the target is stationary (or quasi-stationary) and hence the speckle-averaging condition (2) is not satisfied. In this case, we cannot associate a Collett–Wolf beacon with the return wave. Nevertheless, as already mentioned in Section 1, we can artificially impose a fast change in the return field speckle pattern realizations by rapidly changing (steering) the outgoing beam propagation direction, resulting in the desired displacement of the hit spot at the target surface. This instantaneous hit-spot displacement at the target surface can be described by the beam centroid vector $\mathbf{r}_c(t)$ [see Eq. (18)]. Assume for simplicity that during the time interval $(t_0,t_0+\tau_{\mathrm{ph}})$, the beam centroid moves with a constant velocity along a trajectory

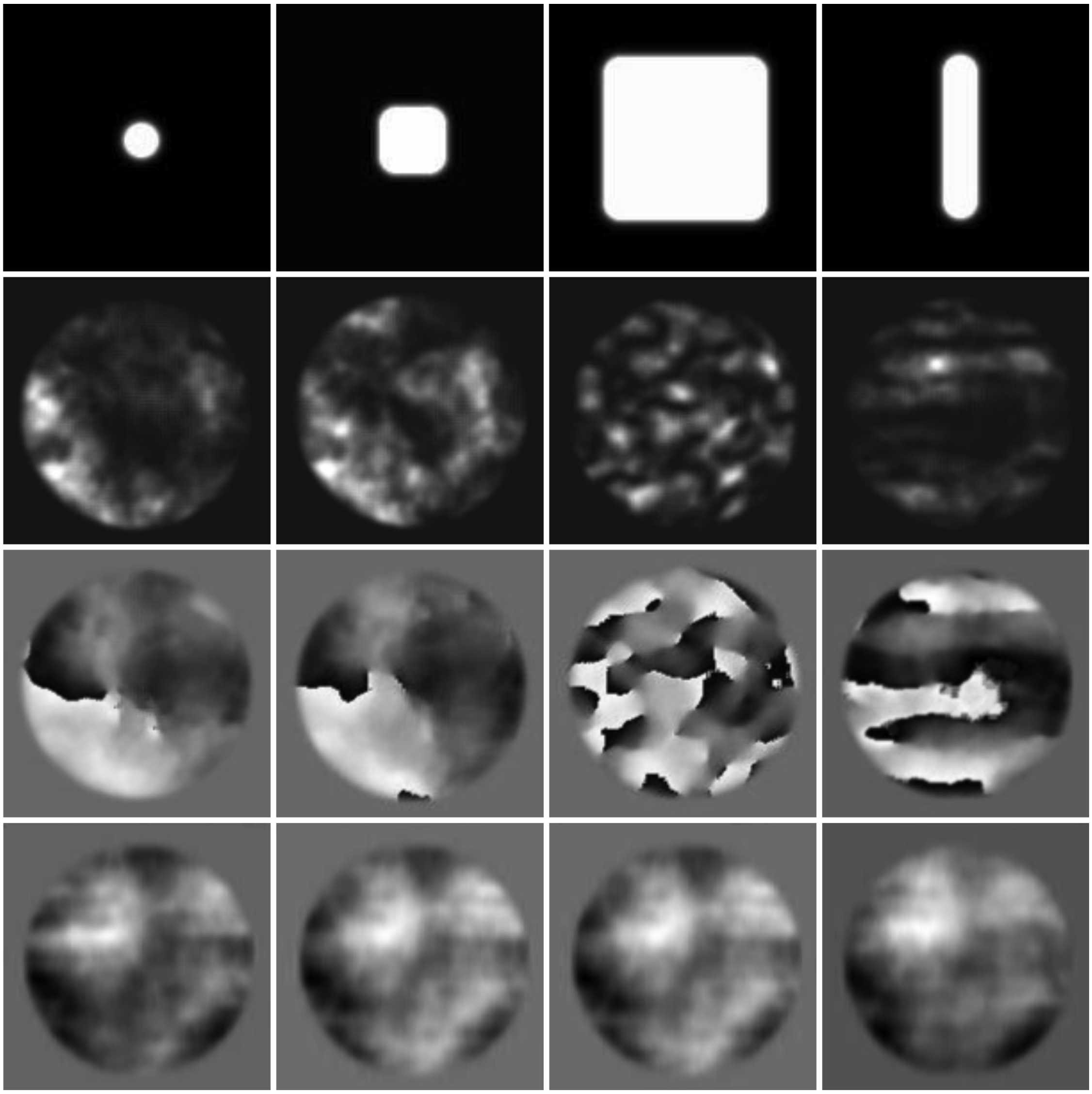

Fig. 1. Stationary beacons (top row) and their impact on the characteristics of the target return wave: the instantaneous speckle-field intensity $|\psi_0(\mathbf{r})|^2$ (second row) and phase $\varphi(\mathbf{r}) = \arg[\psi_0(\mathbf{r})]$ (third row) for the coherent beacons and the SA phase $\Phi(\mathbf{r})$ for the Collett–Wolf beacons (bottom row). Intensity patterns for the beacons are (from left to right) the diffraction-limited (Airy) beacon, square beacons with $b^{\mathrm{sq}} = 2b^{\mathrm{dif}}$ and $b^{\mathrm{sq}} = 4b^{\mathrm{dif}}$, and a cigar beacon with $b^{\mathrm{cg}} = 4b^{\mathrm{dif}}$. The propagation conditions (the set of Kolmogorov phase screens with $D/r_0 = 5$ and the distance to the target $L = 0.05 \times \mathrm{ka}_0^2$) used in computations for all beacons are identical. In phase patterns (third and forth row) are shown with the removed parabolic phase component $\varphi_q(\mathbf{r}) = kr^2/(2L)$.

(hit-spot trajectory) $\mathcal{L}$. Since, for each point $\mathbf{r}_c$ of this trajectory the outgoing beam propagates through a slightly different path, the target-plane intensity distribution $I_T(\mathbf{r}, \mathbf{r}_c, t_0)$ depends on $\mathbf{r}_c$. During the time interval $(t_0, t_0 + \tau_{\mathrm{ph}})$ the Collett–Wolf beacon associated with such hit-spot displacement can then be defined by an averaged intensity $I_T^{\mathcal{L}}(\mathbf{r}, t_0)$ obtained by integrating $I_T(\mathbf{r}, \mathbf{r}_c, t_0)$ along the hit-spot trajectory:

$$I_T^{\mathcal{L}}(\mathbf{r}, t_0) = l^{-1} \int_{\mathcal{L}} I_T(\mathbf{r}, \mathbf{r}_c, t_0) \mathrm{d}l(\mathbf{r}_c), \qquad (27)$$

where $\mathrm{d}l(\mathbf{r}_c)$ is the small element of the hit-spot trajectory of length l at the point $\mathbf{r}_c$. The corresponding Collett–Wolf beacon is then described by the boundary condition for the BF at the target plane:

$$B_L(\boldsymbol{\theta}, \mathbf{R}, t_0) = c I_T^{\mathcal{L}}(\mathbf{R}, t_0). \qquad (28)$$

In the case when the amplitude of the hit-spot displacement is small so that the trajectory $\mathcal{L}$ is located within the isoplanatic path, the Collett–Wolf beacon can be described by the following function:

$$I_T^{\mathcal{L}}(\mathbf{r}, t_0) = l^{-1} \int_{\mathcal{L}} I_T(\mathbf{r} - \mathbf{r}_c, t_0) \mathrm{d}l(\mathbf{r}_c). \qquad (29)$$

The Collett–Wolf beacon can also be created using an auxiliary laser beam. Note that although this beam does not need to share the same optical train with the projected beam, both beams should share the same receiver optical path.

D. Stationary Beacon: Basic Models

Consider several examples of Collett–Wolf beacons. Note that in the target-in-the loop propagation geometry, turbulence-induced refractive index perturbations have a twofold impact on the SA phase. On the one hand, their presence affects the intensity distribution on the target surface $I_T(\mathbf{r},t)$ defining the corresponding Collett–Wolf beacon on which the SA phase $\Phi(\mathbf{r},t)$ depends. On the other hand, refractive index inhomogeneities cause phase aberrations of the return optical wave and hence directly affect both the instantaneous and the SA phase.

To distinguish these two effects, consider first the unidirectional propagation of an optical wave corresponding to a stationary (independent of turbulence) Collett–Wolf beacon. Assume that this beacon is defined by the time-independent (stationary) intensity distribution $I_T(\mathbf{r})$. In the numerical simulations, we considered the following three stationary beacons:

a. Airy beacon—the diffraction-limited beacon described by the target-plane intensity distribution $I_T(\mathbf{r}) = I_T^{\text{Airy}}(\mathbf{r})$ in Eq. (26).

b. Square beacon—the beacon with an intensity pattern in the form of a square of size b^{sq} defined by the following super-Gaussian function

$$I_T(\mathbf{r}) = I_T^{\text{sq}}(\mathbf{r}) \equiv I_T^0 \exp[-(x/b^{\text{sq}})^{16} - (y/b^{\text{sq}})^{16}], \quad (30)$$

where I_T^0 is a constant.

c. Cigar beacon—the beacon defined by the intensity distribution in the form

$$I_T(\mathbf{r}) = I_T^{\text{cg}}(\mathbf{r}) \equiv I_T^{\text{Airy}}(x) \exp[-(y/b^{\text{cg}})^{16}], \quad (31)$$

where $I_T^{\text{Airy}}(x)$ is the Airy function of the coordinate x [see Eq. (26)]. The intensity pattern (31) has the shape of a vertically oriented cigar of width b^{dif} and length $b^{\text{cg}} > b^{\text{dif}}$. Examples of the Airy, square, and cigar beacons are shown in Fig. 1 (top row).

The Airy beacon represents the smallest incoherent Collett–Wolf beacon that can be created at the target surface with the outgoing flat-top beam of diameter D. The square and cigar beacons, as defined by the target-plane intensity distributions (30) and (31), represent models of ideal Collett–Wolf beacons created by rapid steering of the outgoing beam along vertical line of length b^{cg} for the cigar and $x-y$ beam steering with amplitude b^{sq} for the square beacon.

To illustrate the difference between the instantaneous and SA phase, we also analyze unidirectional propagation of the return wave with the complex amplitude at the target plane

$$\psi(\mathbf{r}, z = L) = I_T^{1/2}(\mathbf{r}) \exp[i\xi(\mathbf{r})], \quad (32)$$

where $\xi(\mathbf{r})$ is a random delta correlated on a numerical grid phase function phase and $I_T^{1/2}(\mathbf{r})$ is the target-plane amplitude corresponding to intensity distributions identical to those for the incoherent Collett–Wolf beacons in Eqs. (26), (30), and (31). The condition (32) describes scattering of the collimated laser beam with intensity $I_T(\mathbf{r})$ off the Lambertian surface. Similarly, as the Collett–Wolf beacon is described by the boundary conditions (25) or (28) for the BF, the boundary condition (32) can also be associated with a beacon referred to here as a coherent beacon. For example, the coherent square beacon is defined by Eq. (32) with $I_T(\mathbf{r}) = I_T^{\text{sq}}(\mathbf{r})$. The instantaneous phase corresponding to the coherent beacon is defined as $\varphi(\mathbf{r}) = \arg[\psi_0(\mathbf{r})]$.

E. Instantaneous and SA Phase for an Extended Beacon

In the computation of both instantaneous and speckle-averaged return-wave characteristics corresponding to either a coherent or Collett–Wolf beacon, we used an identical set of 20 equally distanced random Kolmogorov phase screens. The random realization of the phase function $\xi(\mathbf{r})$ in Eq. (32) was identical for all beacons.

Examples of the instantaneous speckle-field intensity $|\psi_0(\mathbf{r})|^2$ and phase $\varphi(\mathbf{r})$ distributions for different coherent beacons are shown in Fig. 1 (second and third rows) as gray-scale patterns. The return-wave intensity distributions (second row) have a well-defined speckle structure. The characteristic speckle size decreases with the increase of the beacon size [18,35].

The corresponding instantaneous phase functions (third row) have a topological structure with the wavefront phase dislocations (branch points) typical for speckle fields [36]. The number of branch points increases with the increase of the beacon size. As mentioned in Section 1, the instantaneous phase is composed of the turbulence-induced phase $\varphi_{\text{at}}(\mathbf{r})$ and the phase component $\varphi_s(\mathbf{r})$ that resulted from the outgoing beam scattering off the target surface (speckle-phase component). As seen from the phase patterns in Fig. 1, the speckle phase component is highly sensitive with respect to the beacon size. Note that the turbulence-induced phase component $\varphi_{\text{at}}(\mathbf{r})$ in Fig. 1 has a small-scale random modulation in a vortex-type phase pattern.

The SA phase patterns in Fig. 1 (bottom row) are quite similar. The SA phase $\Phi(\mathbf{r})$ in this figure does not have branch points and is only weakly dependent on the beacon size and shape. At the same time, the SA phase is highly sensitive to the random realization of refractive index inhomogeneities (phase screen realization). This is contrary to the speckle-field phase whose spatial structure is mainly dependent on target shape, size, and roughness realization.

4. Speckle-Average Phase Conjugation: Numerical Analysis

A. Phase-Conjugate Precompensation for a Stationary Beacon

Compare the efficiency of outgoing beam precompensation using conjugation of either the instantaneous phase $\varphi(\mathbf{r})$ (PC control) or the SA phase $\Phi(\mathbf{r})$ (SA PC control) for the stationary beacons shown in Fig. 1 (top row). In the numerical simulations, we used the outgoing beam with flat-top amplitude $A_0(\mathbf{r})$ [see Eq. (22)] and phase $u(\mathbf{r}) = -\varphi(\mathbf{r})$ for PC and $u(\mathbf{r})$ for SA PC control correspondingly. The same set of phase screens was used for both computation of the phase functions and PC or SA PC precompensation.

Images of the target-plane intensity patterns obtained with conjugation of the speckle-field phase $\varphi(\mathbf{r})$ (top row) and SA phase $\Phi(\mathbf{r})$ (bottom row) are shown in Fig. 2. For all beacons used in the numerical simulations, the SA PC control resulted in significantly better laser beam projection performance (smaller target hit spot) than PC precompensation. Note that the target hit-spot intensity patterns for SA PC control in Fig. 2 are practically independent of the beacon shape. Note that similar calculations performed for circular and rectangular shaped beacons led to similar results. Contrarily, the corresponding intensity distributions for PC precompensation are quite different. For PC control, the increase in beacon size resulted in a noticeable decline in the compensation efficiency (see intensity patterns in the first row in Fig. 2).

The efficiency of PC and SA PC precompensation algorithms can be evaluated using the target-plane metrics—characteristics of the target hit-spot intensity $I_T(\mathbf{r})$. In Fig. 2 this evaluation is based on the Strehl ratio $St = \max[I_T(\mathbf{r})]/\max[I_T^{\text{Airy}}(\mathbf{r})]$ and the normalized sharpness metric J_2 (sharpness function) that is defined as [11]

$$J_2 = \int I_T^2(\mathbf{r})\mathrm{d}^2\mathbf{r} \Big/ \int I_T^{\text{Airy}}(\mathbf{r})\mathrm{d}^2\mathbf{r}. \tag{33}$$

The corresponding values of the St and J_2 metrics are shown in Fig. 2 below the corresponding intensity patterns. Note that the target-plane metrics for SA PC precompensation are approximately equal for all Collett–Wolf beacons shown in Fig. 1 and significantly exceed the corresponding metric values achieved with PC control.

B. SA Phase-Conjugation Based on a Beam Steering-Induced Beacon

Assume now that the Collett–Wolf beacon is created using small amplitude fast steering of the outgoing laser beam. Since, in this case, intensity distribution on the target surface depends on optical inhomogeneities, the corresponding Collett–Wolf beacon is nonstationary. For comparison of nonstationary and stationary beacons, consider steering of the outgoing beam that results in beam centroid displacement along the vertical line of length $b^{\text{cg}} = 4b^{\text{dif}}$. For propagation in vacuum, this beam steering leads to the formation of a stationary cigar beacon similar to one shown in Fig. 1 in the top right corner. In the presence of turbulence, the corresponding nonstationary cigar-type pattern is highly distorted, as demonstrated in Fig. 3(a).

In numerical simulations, the corresponding Collett–Wolf beacon was calculated using multiple integration of the propagation equation (20) for the outgoing beam with flat-top amplitude $A_0(\mathbf{r})$ and M different phase functions

$$u(\mathbf{r}) = u^{(m)}(\mathbf{r}) = u_q(\mathbf{r}) + u_{\text{tilt}}^{(m)}(\mathbf{r}), m = 0, \ldots, M. \tag{34}$$

Here, $u_q(\mathbf{r}) = kr^2/(2L)$ is the quadratic phase corresponding to optimal focusing of the laser beam at the target plane in vacuum and $u_{\text{tilt}}^{(m)}(\mathbf{r}) = k\theta_m y$ are wavefront tilt components corresponding to the

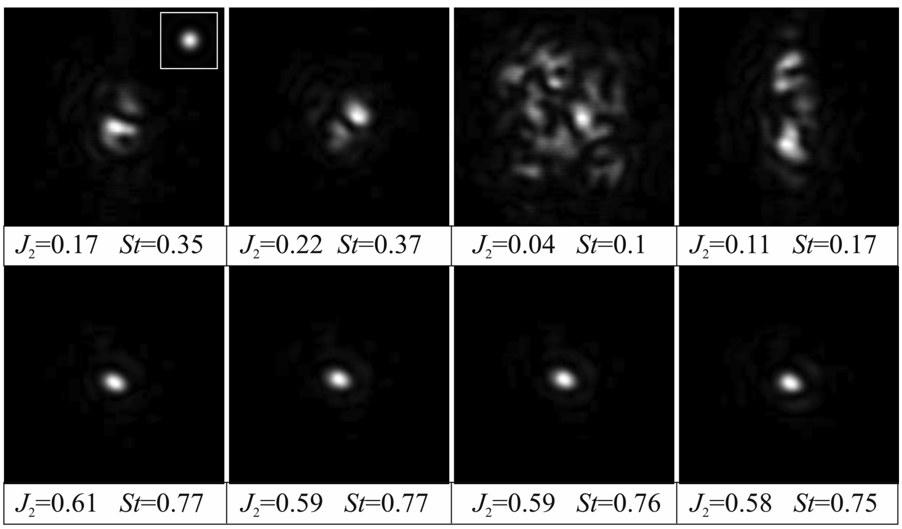

Fig. 2. Target-plane intensity obtained with conjugation of the instantaneous phase (PC control) in the top row and SA phase (SA PC control) in the bottom row for the Airy beacon (first column), square beacon with $b^{\text{sq}} = 2\,b^{\text{dif}}$ (second column) and with $b^{\text{sq}} = 4\,b^{\text{dif}}$ (third column), and for the cigar beacon with $b^{\text{cg}} = 4\,b^{\text{dif}}$ (fourth column). The corresponding patterns of beacon intensity, phase, and SA phase are shown in Fig. 1. The diffraction-limited intensity pattern is shown in the inset. The values of the target-plane metric J_2 and St are given below the corresponding intensity patterns. The propagation parameters are the same as in Fig. 1.

$M+1$ different steering angles $\theta_m = (m - M/2)(\theta_0/M)$. For the target hit-spot trajectory of length b^{cg}, the angular steering amplitude is given by $\theta_0 = b^{sg}/L$. The Collett–Wolf beacon in Fig. 3(a) is obtained by calculating the sum of the target-plane intensity distributions corresponding to $M = 10$ propagation angles θ_m in Eq. (34). The SA phase for this beacon is shown in Fig. 3(b). Note that this phase is similar to the corresponding SA phase pattern in Fig. 1 (right bottom picture) obtained for the stationary cigar beacon of nearly equal length.

The target-plane intensity distribution computed using SA PC wavefront control based on the beam steering-induced (nonstationary) Collett–Wolf beacon is presented in Fig. 3(c). Note that this intensity distribution and the target-plane intensity in Fig. 2 for the stationary cigar beacon are very similar, and the corresponding metric St and J_2 for the stationary and nonstationary cigar beacons are nearly identical.

This result demonstrates that although atmospheric turbulence affects the Collett–Wolf beacon characteristics (shape and brightness), these changes have little effect on SA phase. This suggests that for numerical analysis of SA PC compensation efficiency, the Collett–Wolf beacon that is created by outgoing beam steering can be substituted by a stationary Collett–Wolf beacon with approximately equivalent characteristics. Because direct numerical modeling of outgoing beam steering is extremely computationally expensive, this replacement leads to a significant reduction in computational time.

C. Beacon Anisoplanatism

Assume that the square Collett–Wolf beacon is created by hit-spot scanning inside a square of size b^{sq} at the target plane. The important practical question to answer is: how does the beam steering amplitude b^{sq} that defines the Collett–Wolf beacon size affect SA PC precompensation efficiency? Based on the analysis in Section 4.B, we can avoid time-consuming numerical simulations related to propagation of the steering outgoing laser beam by substituting the nonstationary beacon with a corresponding stationary Collett–Wolf square beacon of size nearly equal to b^{sq}. In the numerical simulations, we used the stationary square beacon defined by Eq. (30).

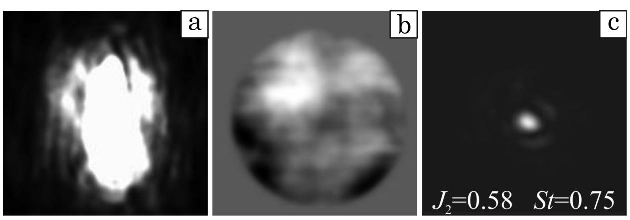

Fig. 3. Speckle-average phase conjugation using the Collett–Wolf beacon created by a small amplitude steering of the outgoing beam. The Collett–Wolf beacon intensity (brightness) pattern in (a) is obtained for the beam steering along the vertical line of length $b^{cg} = 4\,b^{dif}$. This beacon is used for calculation of the SA phase $\Phi(\mathbf{r})$ in (b). The target-plane intensity $I_T(\mathbf{r})$ in (c) is obtained using conjugation of phase $\Phi(\mathbf{r})$. The propagation conditions (phase screens and distance L) are identical in Fig. 1.

For analysis of SA PC precompensation efficiency, we consider the atmospheric-average metrics $\langle St\rangle_{at}$ and $\langle J_2\rangle_{at}$ obtained using different-size square beacons. In the numerical simulations, for each fixed value of the beacon size b^{sq}, the calculations were performed using 20 different realizations of the phase screens and the obtained instantaneous metrics values St and J_2 were averaged.

The dependences $\langle St(b^{sq})\rangle_{at}$ and $\langle J_2(b^{sq})\rangle_{at}$ are shown in Fig. 4 for two different values of the D/r_0 ratio. The decline in SA PC compensation efficiency (decrease in $\langle St\rangle_{at}$ and $\langle J_2\rangle_{at}$ with the increase of the beacon size b^{sq} is related to the beacon anisoplanatism—the propagation conditions for which phase aberration components associated with spherical waves originating from different points of the beacon are uncorrelated and hence cannot be compensated using a single wavefront corrector [8,9,37].

For the beacon with threshold size $b^{sq} = b^{th}$, the metrics values obtained with SA PC compensation are equal to the corresponding values ($\langle St^f\rangle_{at}$ and $\langle J_2^f\rangle_{at}$ in Fig. 4) for an initially focused beam with quadratic phase $u(\mathbf{r}) = u_q(\mathbf{r}) = \mathrm{kr}/(2L)$. SA PC control results in improvement of beam projection efficiency only for a beacon whose size is less than b^{th}. The threshold value b^{th} depends on the turbulence strength as measured by the D/r_0 ratio and decreases as D/r_0 increases. For example, for the Strehl ratio in Figs. 4(a) and 4(b), the beacon size $b^{th} \simeq 7.4b^{dif}$ for $D/r_0 = 5$ and $b^{th} \simeq 6.8b^{dif}$ for $D/r_0 = 8$. Note that for $b^{sq} > b^{th}$, the metric values achieved with SA PC precompensation are smaller than without compensation. This effect can be associated with the negative correlation (decorrelation) between the compensated and residual phase aberrations. This decorrelation vanishes with a further increase of the beacon size.

The numerical analysis shows that the threshold value b^{th} is only weakly dependent on the Collett–Wolf beacon shape and is nearly equal for all beacons examined (the Airy and cigar beacons). This suggests that the decline in the metrics values in Fig. 4 is related to the anisoplanatic effect.

To link directly the beacon size b^{sq} with a characteristic anisoplanatic patch length l_{is}, consider a small-size (unresolved) reference light source located in the coordinate origin of the target plane (on-axis coherent beacon). In the numerical simulations, this beacon was defined by the boundary condition (30), with $\xi(\mathbf{r}) = 0$ and $I_T(\mathbf{r}) = I_T^0 \exp(-r^2/b_{ref}^2)$, where $b_{ref} = 0.25\,b^{dif}$ is the beacon width. Instantaneous phase $\varphi_{ref}(\mathbf{r})$ of an optical wave originating from this reference beacon was calculated by integrating the propagation equation (21) from the target to the transceiver plane.

The conjugated phase $-\varphi_{ref}(\mathbf{r})$ was used for atmospheric turbulence precompensation of the outgoing beam. Anisoplanatic propagation conditions similar

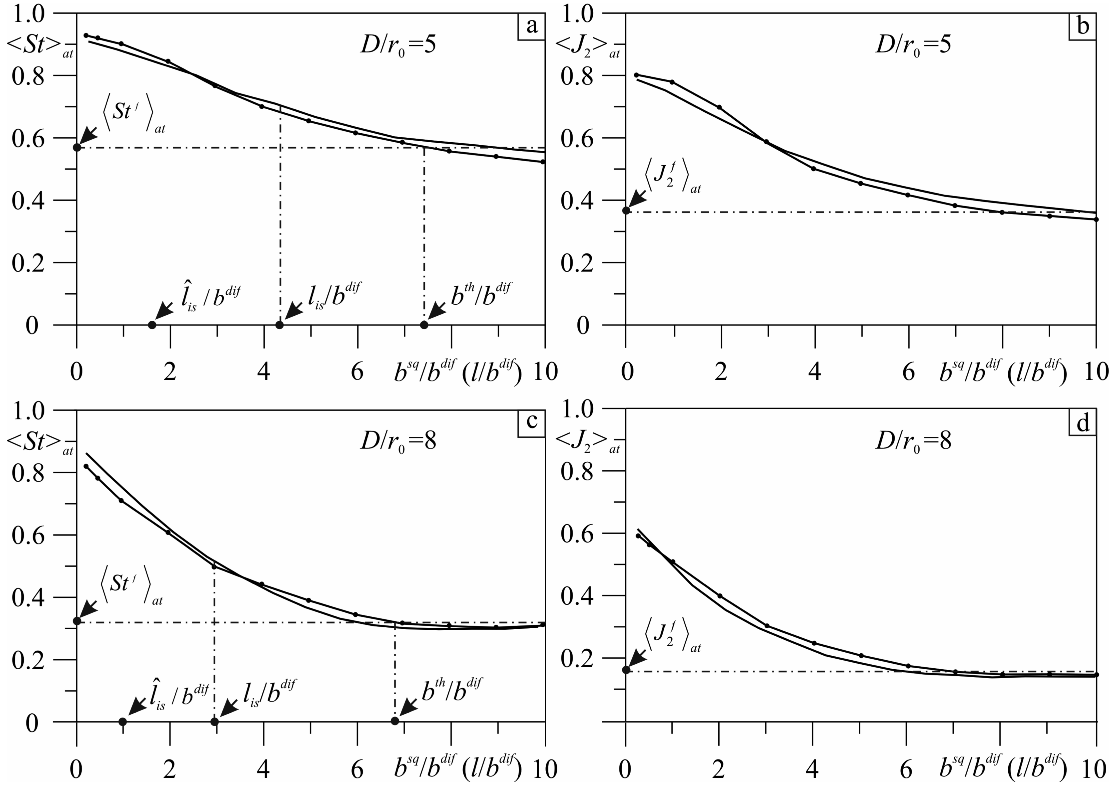

Fig. 4. Impact of anisoplanatism on the outgoing beam precompensation efficiency using a square Collett–Wolf for SA PC (lines with dots) and an unresolved coherent Gaussian beacon for PC (solid lines) control for $D/r_0 = 5$ (a), (b) and $D/r_0 = 8$ (c), (d). Atmospheric-average metrics $\langle \mathrm{St} \rangle_{\mathrm{at}}$ in (a), (c) and $\langle J_2 \rangle$ in (b), (d) are shown as functions of the beacon size b^{sq} for the SA PC precompensation and displacement l (distance between the location of the unresolved beacon and the outgoing beam aim point at the target plane) for the PC control. The horizontal lines correspond to the outgoing beam that is focused on the target. The threshold beacon size b^{th}, the isoplanatic distance l_{is} that is defined by the e^{-1} fall-off of the Strehl ratio, and $\hat{l}_{\mathrm{is}} = 0.57\, r_0$ are normalized on the diffraction-limited beam radius b^{dif} (Airy radius) for the flat-top beam of radius a_0 in vacuum. The propagation conditions (phase screens and distance L) are identical in Fig. 1.

to the extended Collett–Wolf beacon are created by considering off-axis propagation of the PC precompensated outgoing beam with the following phase:

$$u(\mathbf{r}) = -\varphi_{\mathrm{ref}}(\mathbf{r}) + u_{\mathrm{tilt}}(\mathbf{r}), \tag{35}$$

where $u_{\mathrm{tilt}}(\mathbf{r}) = k(l/L)x$ is the wavefront tilt component that results in beam centroid displacement in vacuum at distance l. Wavefront phase (35) corresponds to off-axis propagation of the outgoing beam with precompensation based on conjugation of phase $\varphi_{\mathrm{ref}}(\mathbf{r})$ obtained for an on-axis unresolved beacon.

In the numerical simulations, for adequate comparison of SA PC precompensation based on the square Collett–Wolf and reference beacons, the same set of phase screens was used.

The obtained dependences of metrics $\langle St \rangle_{\mathrm{at}}$ and $\langle J_2 \rangle_{\mathrm{at}}$ on the normalized displacement distance l/b^{dif} are compared in Fig. 4 with the corresponding dependences for the square Collett–Wolf beacon. Note that the displacement distance l/b^{dif} can be directly associated with the normalized size $b^{\mathrm{sq}}/b^{\mathrm{dif}}$ of the Collett–Wolf beacon.

The strength of anisoplanatism can be evaluated using $\exp(-1)$ fall off in metric $\langle St \rangle_{\mathrm{at}}$ as illustrated in Fig. 4(a). The corresponding value of the displacement l defines the isoplanatic patch length l_{is} (isoplanatic distance). As seen in Figs. 4(a) and 4(b), the isoplanatic distance $l_{\mathrm{is}} \simeq 4.2 b^{\mathrm{dif}}$ for $D/r_0 = 5$ and $l_{\mathrm{is}} \simeq 2.9 b^{\mathrm{dif}}$ for $D/r_0 = 8$. Note that the obtained isoplanatic distances l_{is} are noticeably larger compared with the corresponding distances $\hat{l}_{\mathrm{is}}$ calculated based on the commonly used expression $\hat{l}_{\mathrm{is}} = 0.57\, r_0$ that is derived from the analysis of the correlation between the on- and off-axis phase aberrations [29,37–39].

Note that the dependences $\langle St(\mathrm{l}) \rangle_{\mathrm{at}}$ and $\langle J_2(\mathrm{l}) \rangle_{\mathrm{at}}$ obtained for an unresolved reference beacon and the corresponding dependences $\langle St(b^{\mathrm{sq}}) \rangle_{\mathrm{at}}$ and $\langle J_2(b^{\mathrm{sq}}) \rangle_{\mathrm{at}}$ for the square Collett–Wolf beacon nearly coincide. This indicates that the decline in SA PC precompensation efficiency with the increase of the Collett–Wolf beacon size is directly related to the beacon anisoplanatism.

The negative impact of anisoplanatism can be decreased with the use of a small-size Collett–Wolf beacon by decreasing the beam scanning amplitude. Nevertheless, since the SA phase should be measured using a large number of statistically independent speckle-field realizations, the scanning amplitude decrease has a certain limitation. The scanning amplitude lower limit is quite difficult to estimate from numerical simulations. In Section 4 this estimation is performed using bench-top experiments with a SA PC control system. The experimental results demonstrate that SA PC precompensation can be efficient even if the Collett–Wolf beacon size is nearly equal or even less than the diffraction-limited beam size.

D. SA PC Control for Rapidly Moving Lambertian Surface

Consider SA PC control of the outgoing beam for a target with a fast moving Lambertian surface so that the speckle-averaging condition (2) is satisfied without beam steering. A nonstationary Collett–Wolf beacon is then defined by the intensity distribution at the target surface. The SA PC precompensation then results in an iterative sequence of wavefront phase $u(\mathbf{r}, t_n)$ updates at time $t = t_n = n\Delta t$, where $n = 1, 2..$, is the iteration number, and $\Delta t = \tau_{\mathrm{AO}}$ is the time delay between subsequent SA PC iterations. Assume that optical inhomogeneities can be considered as frozen during the first N_{PC} SA PC iterations so that $N_{\mathrm{PC}}\Delta t < \tau_{\mathrm{at}}$. For the complex amplitude of the outgoing beam at the SA PC $n+1$st iteration, we have

$$A(\mathbf{r}, z = 0, t_{n+1}) = A_0(\mathbf{r}) \exp[-i\Phi(\mathbf{r}, t_n)], \qquad (36)$$

where $\Phi(\mathbf{r}, t_n)$ is the SA phase at the nth iteration.

In the numerical analysis, the cycle (adaptation trial) of $N_{\mathrm{PC}} = 10$ SA PC iterations (36) was performed for a fixed set of phase screens. Dynamics of the SA PC precompensation process during the adaptation trial are characterized by the dependences $St(n)$ and $J_2(n)$ referred to here as the adaptation curves.

The adaptation trials were repeated a number of times with a different set of phase screens to obtain atmospheric-average SA PC adaptation curves $\langle St(n)\rangle_{\mathrm{at}}$ and $\langle J_2(n)\rangle_{\mathrm{at}}$. The adaptation curves corresponding to the atmospheric-average metric $\langle J_2(n)\rangle_{\mathrm{at}}$ are presented in Fig. 5 for both initially collimated (solid lines) and focused (dotted lines) beams and different D/r_0 values. The averaging is performed over a set of $M = 50$ statistically independent atmospheric phase-distorting layers.

The adaptation curves in Fig. 5 show that SA PC precompensation results in a noticeable increase in the target-plane metric $\langle J_2\rangle_{\mathrm{at}}$. A major contribution to this increase in the metric for the collimated beam comes from compensation of the initial beam divergence. For an initially focused beam, the increase in metric $\langle J_2\rangle_{\mathrm{at}}$ is solely due to compensation of the turbulence-induced phase aberrations. The compensation gain as measured by the ratio $g(n) = \langle J_2(n)\rangle_{\mathrm{at}}/\langle J_2(n=0)\rangle_{\mathrm{at}}$ increases with D/r_o and for an initially focused beam reaches its maximum value $g(n = 20) \cong 2.5$ for $D/r_0 = 4.0$. With a further increase in turbulence strength, the efficiency of SA PC precompensation gradually drops.

The pictures of the target-plane intensity distributions in Figs. 5(a) through 5(d) show that phase SA PC precompensation can significantly increase the

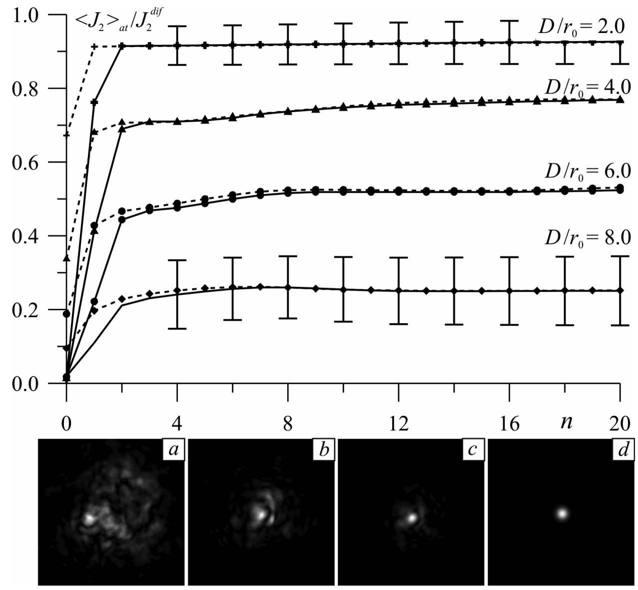

Fig. 5. Efficiency of phase control based on SA PC control for laser beam projection onto an extended target with rapidly moving Lambertian surface. Dependence of the atmospheric-average target-plane metric $\langle J_2\rangle_{\mathrm{at}}$ on SA PC iteration number n for different D/r_0: solid lines—initial plane phase $u(\mathbf{r}, 0) = 0$; dotted lines—focused beam with $u(\mathbf{r}, 0) = u_q(\mathbf{r}) = kr^2/(2L)$. The propagation distance is $L = 0.2\,\mathrm{ka}_0^2$, where a_0 is the outgoing flat-top beam radius. Phase distortions are modeled by $N = 20$ equidistant Kolmogorov phase screens. Gray-scale images correspond to target-plane intensity distributions: (a) and (b) prior to compensation for $D/r_0 = 6.0$; (a) with $u(\mathbf{r}, 0) = 0$ and (b) with $u(\mathbf{r}, 0) = u_q(\mathbf{r})$; (c) and (d) SA PC for $n = 5$, (c) for $D/r_0 = 6.0$ and (d) for $D/r_0 = 0.2$.

target hit-spot brightness in the conditions that conventional PC and FC beam control techniques fail—laser beam projection through a distributed phase-distorting medium onto an extended moving (spinning) target or in the presence of strong beam jitter.

5. Adaptive Control with Collett–Wolf Beacon: Experimental Results

A. Experimental Setup

In this section we describe the results of the proof-of-concept bench-top experiments with an adaptive wavefront control system based on a Collett–Wolf beacon. In the system schematic in Fig. 6 the argon ($\lambda_p = 0.53\,\mu$m) and He–Ne ($\lambda_b = 0.63\,\mu$m) lasers are used as the coherent light sources for the projected and beacon beams, respectively.

The system optimizes the power density (hit-spot brightness) of the projected laser beam on an extended target with a randomly rough surface using conjugation of the SA phase. The SA phase is reconstructed from the SA wavefront slopes measured with a conventional SH wavefront sensor (CLAS-2D from Wavefront Sciences Inc.). The Collett–Wolf beacon used for measurements of the SA slopes is created by steering (scanning) the auxiliary laser beam (beacon beam). For beam steering, the harmonic signals (control voltages) alternating with frequency $f \sim 800$ Hz are applied to the actuators of the tip/tilt (beam steering) mirror. The beam steering results in fast displacement of the beacon laser hit spot within a target region (Collett–Wolf beacon region) of size b_{scan}. The hit-spot scanning amplitude b_{scan} (on the order of $b^{\text{dif}} < b_{\text{scan}} < 10\, b^{\text{dif}}$, where $b^{\text{dif}} \simeq 25\,\mu\text{m}$ and velocity of its centroid displacement v_T (on the order of $5-10\,\text{cm/s}$) are controlled by changing the amplitude of the applied control voltages. The Collett–Wolf beacon and the hit spot of the nonscanning beam projected onto the target are overlapped as shown in Fig. 6(g).

In the optical system schematic in Fig. 6, the input beacon laser beam (diameter 10 mm) is first reflected from the tip/tilt (beam steering) mirror and then is combined with the projected laser beam. The optical relay system (lenses L_1 and L_2) expands both beams up to 25 mm in diameter. The expanded beams are reflected from the deformable mirror (*DM*) located in the image plane of the tip/tilt mirror and are focused by the off-axis parabolic mirror (focal distance 38 cm) onto an extended target (flat end of an aluminum cylinder), which is shown in Fig. 6(a). A small portion of the focused beams is redirected by the beam splitter BS_1 to the camera (CCD_1) located at the plane conjugated to the target surface. The speckle fields that scatter off the target propagate back and, after reflection from the *DM* and the beam splitter BS_2, enter the receiver system. The receiver system is composed of the imaging lens L_3 with the camera (CCD_2), which images the target surface through the *DM*, the optical relay system (lenses L_4 and L_5), and the Shack–Hartmann wavefront sensor (SH WFS). The pupil plane of the wavefront sensor is located in the conjugate plane for both the deformable and tip/tilt mirrors. The integration time of the SH WFS photoreceiver ($\tau_{\text{ph}} = 128\,\mu\text{s}$) is set sufficiently longer than the characteristic time of speckle-field realization update ($\tau_s = b_{\text{scan}}/v_T \sim 1.0\,\text{ms}$), so that the SH WFS measures the speckle-averaged wavefront slopes of the scanning beacon beam. The SH WFS used in the experiments had a lenslet array composed of 68×68 lenslets with focal length 4.6 mm.

The bandpass optical filters located in front of the target imaging camera (CCD_1), imaging lens L_3, and optical relay system (L_4 and L_5) allow analysis of the outgoing or return waves originating from either the beacon or projected laser beams or from both simultaneously.

The phase aberrations are introduced into the system by applying random voltages to all 13 electrodes of the semi-passive bimorph-type continuously *DM*. The geometry of the *DM* electrodes is shown in Fig. 6(b). The example of the target-plane intensity distribution (hit-spot intensity pattern) of the projected laser beam corresponding to the random applied voltages in Fig. 6(c) is compared with the corresponding intensity pattern in Fig. 6(d) for the compensated beam.

The characteristic patterns of the Collett–Wolf beacons used in the experiments are shown in Figs. 6(e) and 6(g). The cigar [Fig. 6(e)] and square

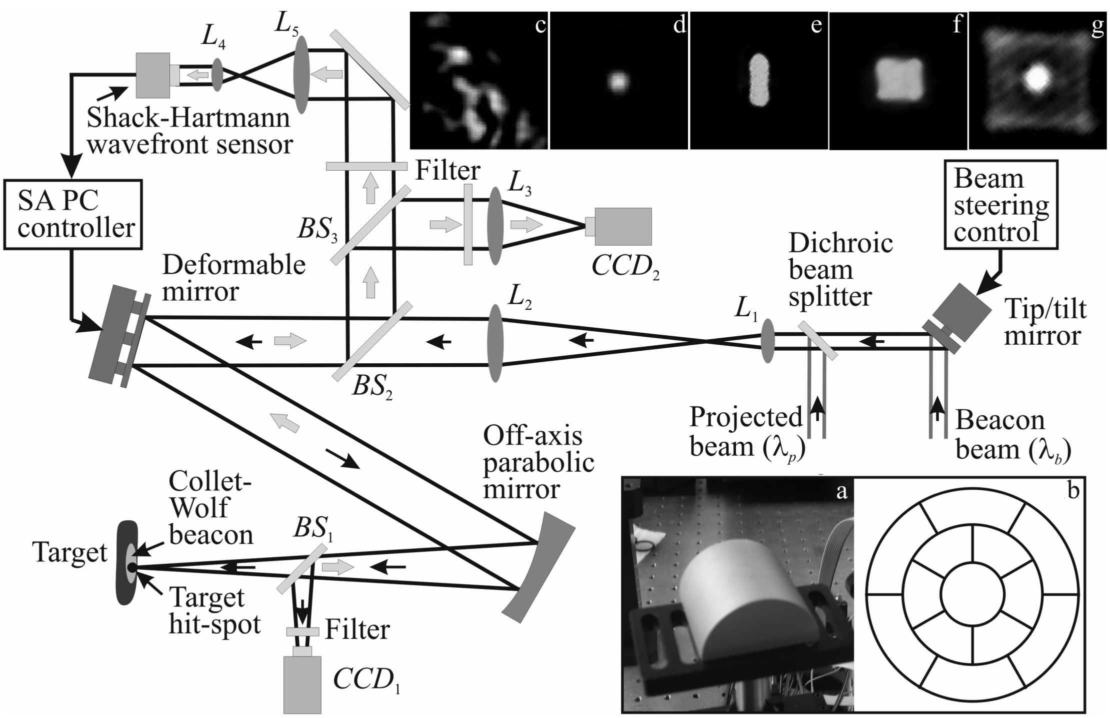

Fig. 6. Schematic of the bench-top adaptive optical system for laser beam projection on an extended target based on SA PC feedback control. Insets are image of the target (a), geometry of the deformable mirror (*DM*) electrodes (b), target-plane intensity of the projected beam without (c) and without (d) adaptive compensation of a random phase aberrations, the long-exposure intensity distribution of the beacon beam with one (e) and two-dimensional (f) scanning, and the projected beam (bright spot in the middle) inside the square Collett–Wolf beacon created by two-dimensional scanning of the beacon laser beam (g). The images in (c)—(g) correspond to a $110 \times 110\,\mu\text{m}$ area.

[Fig. 6(f)] patterns of the beacon beam are obtained with the target imaging camera (CCD_1) and the bandpass filter that cuts off the light from the argon laser (projected laser beam). The corresponding image with the filter removed in Fig. 6(g) shows the square Collett–Wolf beacon with the hit spot of the projected beam in the center of the beacon. The camera integration time is $\tau_{\text{ph}} = 30\,\text{ms}$.

B. Instantaneous and SA Phase Measurements

The random phase aberrations that are introduced by the *DM* result in the corresponding changes in both the outgoing and return waves. The characteristic examples of the return speckle-field intensity and phase distributions of the projected beam are shown in Figs. 7(a) and 7(b). Both patterns are obtained using the SH wavefront sensor with the bandpass filter that blocks the light from the beacon laser. The strong spatial modulation in the intensity pattern seen in Fig. 7(a) results in significant errors in the reconstructed phase shown by the set of random black regions in Fig. 7(b).

For the SA phase measurements, the bandpass filter was replaced by a filter that only passes the scattered light originating from the scanning beacon beam. In this case, due to a relatively long integration time, the SH wavefront sensor camera measured the SA slopes. Two examples of the SA phase that is reconstructed from the speckle-averaged slopes are shown in Figs. 7(c) and 7(d). These SA phase patterns are obtained using identical random phase aberrations but different Collett–Wolf beacons [cigar and square Collett–Wolf beacons shown in Figs. 6(e) and 6(f)]. Contrary to the instantaneous phase in Fig. 7(b), the SA phase patterns obtained for the Collett–Wolf beacons are nearly identical.

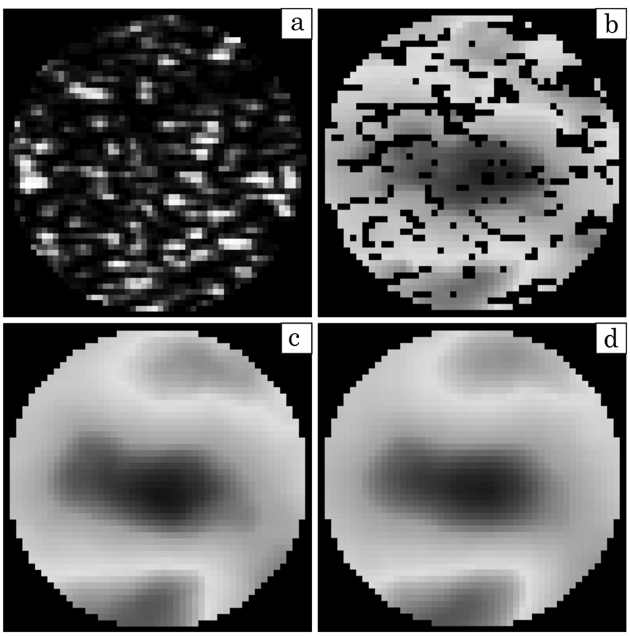

Fig. 7. Impact of phase aberration on the return speckle-field intensity (a) and instantaneous phase (b) for the projected beam, and on the SA phase (c), (d) obtained for the beacon beam with one- (c) and two-dimensional (d) scanning.

C. Adaptive Control Based on a Beam Scanning-Induced Beacon

Consider the experimental results of adaptive precompensation of static random phase aberrations using PC and SA PC algorithms. In the experiments, a set of $N_{\text{ab}} = 20$ different realizations of random voltages were sequentially applied to the *DM* electrodes to create statistically independent phase aberration realizations. Compensation of each aberration was performed using either PC or SA PC adaptation trials, each composed of $N_{\text{PC}} = 10$ iterations.

For PC control, the return wave corresponding to the projected beam that scatters off the target was used as the input for the SH WFS. The reconstructed phase $\varphi_n(\mathbf{r})$ at the nth iteration $(n = 1, \ldots, N_{\text{PC}})$ was used to calculate the coefficients $\{c_j^{(n)}\}(j = 1, \ldots, 13)$ of phase $\varphi_n(\mathbf{r})$ deconvolution over the *DM* response functions $\{S_j(\mathbf{r})\}$. The response functions were preliminarily measured using a Zygo interferometer. The coefficients $\{c_j^{(n)}\}$ were used for the control voltage update in the form $u_j^{(n+1)} = u_j^{(n)} - c_j^{(n)}$, $((j = 1, \ldots, 13)$, where $\{u_j^{(n)}\}$ are the control voltages at the *DM* electrodes at the nth iteration. The iterative update of the control voltages resulted in the corresponding change in the target-plane intensity distribution of the projected beam as registered by the target-plane camera (CCD_1 in Fig. 6). During each adaptation trial, precompensation efficiency was estimated by the Strehl ratio St. The dependences $St(n)$, $n = 1, \ldots, N_{\text{PC}}$ obtained for $N_{\text{ab}} = 20$ different phase aberrations were averaged. The corresponding averaged adaptation curve $\langle St(n) \rangle$ for PC wavefront control is shown in Fig. 8. Note that the average value of the Strehl ratio achieved after N_{PC} PC iterations is relatively low $[\langle St(N_{\text{PC}}) \rangle \sim 0.45]$. At the same time, the level of the Strehl ratio fluctuations, as characterized by standard deviation and shown in Fig. 8 by vertical bars, is large (~45%).

Consider now the corresponding results obtained using the SA PC control algorithm. For phase distortion generation, a set of identical random control voltages was used for both PC and SA PC control. The square Collett–Wolf beacon of size $b^{\text{sq}} \cong 4\,b^{\text{dif}}$ was created by the two-dimensional steering of the beacon beam. This Collett–Wolf beacon was used for measurements of the SA slopes and reconstruction of the SA phase functions $\{\Phi_n(\mathbf{r})\}(n = 1, \ldots, N_{\text{PC}})$ at each iteration of the SA PC precompensation trial.

Similarly to the PC-based precompensation, the controls $\{c_j^{(n)}\}$ at the nth iteration were obtained by deconvolution of the SA phase $\Phi_n(\mathbf{r})$ over the wavefront corrector response functions $\{S_j(\mathbf{r})\}$. In Fig. 8 the dependence of the Strehl ratio on the iteration number $\langle St(n) \rangle$ for SA PC phase aberration compensation is compared with the corresponding dependence for PC control. The averaging is performed over $N_{\text{ab}} = 20$ adaptation trials. Note that both PC and SA PC adaptation curves in this figure

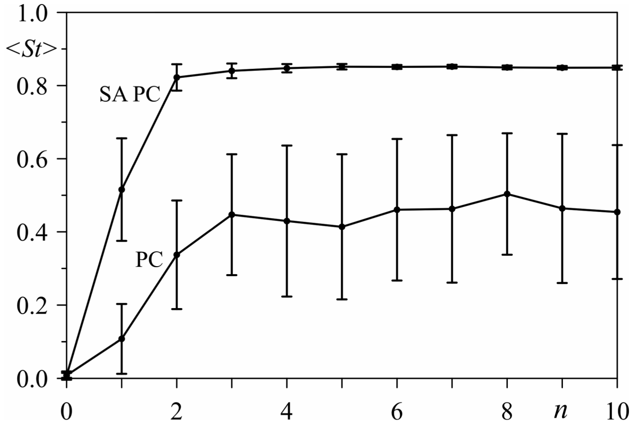

Fig. 8. Dependence of the averaged Strehl ratio $\langle St \rangle$ on the iteration number n obtained in the phase distortion compensation experiments with PC and SA PC feedback control of wavefront phase for the laser beam projected onto an extended stationary target in Fig. 6(a). Phase distortions are created by applying random voltages to the deformable mirror (*DM*) electrodes. Averaging is performed using a set of 20 different phase aberration patterns. Two-dimensional scanning of the beacon was used to generate the square Collett–Wolf beacon shown in Fig. 6(g). The length of vertical bars indicates the standard deviation in the Strehl ratio.

correspond to the Strehl ratio for the projected beam, although the SA phase was measured using the scanning beacon beam. An example of the target-plane intensity distribution (hit-spot intensity) obtained at the end of the SA PC adaptation trial is shown in Fig. 6(d). The presented data clearly demonstrate the advantage of the SA PC-based precompensation technique. The averaged Strehl ratio value achieved using SA PC control ($\langle St(N_{\mathrm{PC}}) \rangle \sim 0.82$) is nearly twice as high as that achieved with the PC control algorithm. Note that the residual uncompensated phase error is mostly related to the presence of high-order aberrations that cannot be compensated with the *DM* used.

The standard deviation of the Strehl ratio fluctuations is significantly smaller for SA PC than for the conventional PC control algorithm (compare vertical bars for the curves in Fig. 8).

The performance of SA PC control (average Strehl ratio $\langle St(N_{\mathrm{PC}}) \rangle$) remained practically unchanged within a wide range of beacon beam scanning amplitudes ($b^{\mathrm{dif}} \le b_{\mathrm{scan}} \le 8b^{\mathrm{dif}}$) and began to decrease gradually as scanning (either one- or two-dimensional) amplitude decreased beyond b^{dif} and above $8\,b^{\mathrm{dif}}$–$10\,b^{\mathrm{dif}}$. Note that since phase aberrations are induced and compensated using the *DM* located in the beam projection system pupil plane, the propagation path of the projected beam, including the beacon generated by beam steering, is isoplanatic. For this reason, the decrease in the average Strehl ratio $\langle St \rangle$ for large scanning amplitudes ($b_{\mathrm{scan}} > 8\,b^{\mathrm{dif}}$) observed in the experiments is related to additional phase aberrations caused by off-axis propagation of the scanning beacon beam through the system optical train.

6. Conclusion

In this paper, we consider an adaptive laser beam projection system that uses a new type of reference light source (beacon) for wavefront measurements and atmospheric turbulence effects compensation. This reference source—identified here as the Collett–Wolf beacon—is artificially created directly at the extended target with a randomly rough surface using a rapid steering (scanning) auxiliary (beacon) laser beam. Steering of the beacon beam leads to rapid displacement of the laser beam hit spot inside a small region of the target that defines the Collett–Wolf beacon size, and thus results in the rapid update of the scattered off the target surface return speckle-field realizations inside the wavefront sensor receiver aperture. The wavefront sensor (Shack–Hartmann sensor) measures wavefront slopes of the return field that are averaged over a large number of speckle-field realizations. We assume that this speckle averaging can be performed over a relatively short time so that the atmospheric turbulence-induced optical inhomogeneities can be considered as frozen (speckle-averaging condition). It is shown that the function that is computed from the SA slopes using conventional phase reconstruction techniques, referred to here as the SA phase, can be directly utilized for phase-conjugate type precompensation of the outgoing beam phase. The numerical simulations show that the Collett–Wolf beacon-based adaptive optics technique can potentially provide efficient compensation of turbulence effects, resulting in an increase of the projected laser beam power density on a remote extended target in volume turbulence.

Scanning of the laser beam projected onto the target results in partial averaging of the atmospheric turbulence-induced phase distortions within the propagation medium volume of the beacon beam, leading to the decline of compensation efficiency. As we show, this effect is directly associated with anisoplanatism. Nevertheless, since the Collett–Wolf beacon is located directly at the target surface, the Collett–Wolf beacon-based AO approach does not suffer from conical anisoplanatisms as does the laser guide-star AO technique. Besides the Collett–Wolf beacon can be in principle created at any target independently of its elevation angle and height above the ground.

Similarly to the laser guide-star technique, the wavefront measurements with the Collett–Wolf beacon cannot provide absolute wavefront tilt information and hence cannot stabilize the hit spot of the projected beam at the target surface.

This work was supported by the U.S. Joint Technology Office under contract JTO-07-S&A-0238 and by the Cooperative Agreement W911NF-06-2-0009 between the U.S. Army Research Laboratory and the University of Maryland, College Park. The authors are grateful to A. Kohnle for helpful discussions and K. Aschenbach for technical support.

References

1. J. W. Hardy, eds., *Adaptive Optics for Astronomical Telescopes* (Oxford University Press, 1998).
2. M. A. Vorontsov, A. V. Koriabin, and V. I. Shmalhauzen, eds., *Controlling Optical Systems* (Nauka, 1988).
3. B. Ya. Zeldovich, N. F. Pilipetsky, and V. V. Shkunov, eds., *Principles of Phase Conjugation* (Springer, 1985).
4. R. A. Fisher, ed., *Optical Phase Conjugation* (Academic, 1983).
5. R. K. Tyson, ed., *Principles of Adaptive Optics* (Academic, 1991).
6. J. H. Shapiro, "Reciprocity of the turbulent atmosphere," J. Opt. Soc. Am. **61**, 492–495 (1971).
7. M. A. Vorontsov, V. V. Kolosov, and A. Kohnle, "Adaptive laser beam projection on an extended target: phase- and field-conjugate precompensation," J. Opt. Soc. Am. A **24**, 1975–1993 (2007).
8. N. V. Vysotina, N. N. Rozanov, V. E. Semenov, and V. A. Smirnov, "Amplitude-phase adaptive control over optically inhomogeneous paths with deformable mirrors," Izv. Vysshikh Uchebnykh Zavedenii, Fizika **11**, 42–50 (1985).
9. J. D. Barchers, "Closed-loop stable control of two deformable mirrors for compensation of amplitude and phase fluctuations," J. Opt. Soc. Am. A **19**, 926–945 (2002).
10. T. R. O'Meara, "The multidither principle in adaptive optics," J. Opt. Soc. Am. **67**, 306–315 (1977).
11. R. A. Miller and A. Buffington, "Real-time correction of atmospherically degraded telescope images through image sharpening," J. Opt. Soc. Am. **64**, 1200–1210 (1974).
12. M. A. Vorontsov, G. W. Carhart, D. V. Pruidze, J. C. Ricklin, and D. G. Voelz, "Image quality criteria for an adaptive imaging system based on statistical analysis of the speckle field," J. Opt. Soc. Am. A. **13**, 1456–1466 (1996).
13. P. Piatrou and M. Roggemann, "Beaconless stochastic parallel gradient descent laser beam control: numerical experiments," Appl. Opt. **46**, 6831–6842 (2007).
14. M. A. Vorontsov and V. I. Shmalhauzen, eds., *Principles of Adaptive Optics* (Nauka, 1985).
15. N. C. Mehta and C. W. Allen, "Dynamic compensation of atmospheric turbulence with far-field optimization," J. Opt. Soc. Am. A **11**, 434–443 (1994).
16. S. A. Kokorowski, M. E. Pedinoff, and J. E. Pearson, "Analytical, experimental, and computer simulation results on interactive effects of speckle with multidither adaptive optics systems," J. Opt. Soc. Am. **67**, 333–345 (1977).
17. M. A. Vorontsov, V. N. Karnaukhov, A. L. Kuz'minskii, and V. I. Shmalhauzen, "Speckle effects in adaptive optical systems," Sov. J. Quantum Electron. **14**, 761–766 (1984).
18. V. V. Dudorov, M. A. Vorontsov, and V. V. Kolosov, "Speckle-field propagation in "frozen" turbulence: brightness function approach," J. Opt. Soc. Am. A **23**, 1924–1936 (2006).
19. J. E. Pearson, S. A. Kokorowski, and M. E. Pedinoff, "Effects of speckle in adaptive optical systems," J. Opt. Soc. Am. **66**, 1261–1267 (1976).
20. M. A. Vorontsov and G. W. Carhart, "Adaptive phase distortion correction in strong speckle-modulation conditions," Opt. Lett. **27**, 2155–2157 (2002).
21. M. A. Vorontsov and V. Kolosov, "Target-in-the-loop beam control: basic considerations for analysis and wave-front sensing," J. Opt. Soc. Am. A **22**, 126–141 (2005).
22. R. R. Parenti and R. J. Sasiela, "Laser-guide-star systems for astronomical applications," J. Opt. Soc. Am. A **11**, 288–309 (1994).
23. D. L. Fried and J. F. Belsher, "Analysis of fundamental limits of artificial-guide-star adaptive-optics system performance for astronomical imaging," J. Opt. Soc. Am. A. **11**, 277–287 (1994).
24. N. Ageorges and C. Dainty, eds., *Laser Guide Star Adaptive Optics for Astronomy* (Kluwer Academic, 2000).
25. E. Collett and E. Wolf, "Is complete coherence necessary for generation of highly directional light-beams?" Opt. Lett. **2**, 27–29 (1978).
26. L. Mandel and E. Wolf, eds., *Optical Coherence and Quantum Optics* (Cambridge University Press, 1995).
27. F. Gori, "Mode propagation of the field generated by Collett–Wolf Schell-model sources," Opt. Commun. **46**, 149–154 (1983).
28. G. Rousset, "Wave-front sensors," in *Adaptive Optics in Astronomy*, F. Roddier, ed. (Cambridge University Press, 1999), pp. 91–130.
29. We assume here that the obtained vector-function $\boldsymbol{\alpha}(\mathbf{r}, t)$ represents a path-independent vector field (at least at compact areas of receiver aperture).
30. M. C. Rytov, Yu A. Kravtsov, and V. I. Tatarskii, eds., *Principles of Statistical Radiophysics 4, Wave Propagation Through Random Media* (Springer-Verlag, 1989).
31. F. G. Bass and I. M. Fuks, eds., *Wave Scattering from Statistically Rough Surfaces* (Pergamon, 1979).
32. J. W. Goodman, *Introduction to Fourier Optics* (McGraw-Hill, 1988).
33. I. Tatarskii, *Wave Propagation in a Turbulent Medium* (McGraw-Hill, 1961).
34. D. L. Fried, "Statistics of a geometric representation of wavefront distortion," J. Opt. Soc. Am. **55**, 1427–1435 (1965).
35. J. C. Dainty, ed., *Laser Speckle and Related Phenomena*, 2nd ed. (Springer-Verlag, 1984).
36. D. L. Fried, "Branch point problem in adaptive optics," J. Opt. Soc. Am. A, **15**, 2759–2768 (1998).
37. M. C. Roggemann and B. M. Welsh, *Imaging Through Turbulence* (CRC Press, 1996).
38. D. L. Fried, "Anisoplanatism in adaptive optics," J. Opt. Soc. Am. **72**, 52–61 (1982).
39. B. M. Welsh and C. S. Gardner, "Effects of turbulence-induced anisoplanatism on the imaging performance of adaptive-astronomical telescopes using laser guide stars," J. Opt. Soc. Am. A **8**, 69–80 (1991).